

## Research Article

# Topographic Effects on the Seismic Response of Trapezoidal Canyons Subjected to Obliquely Incident SV Waves

Hui Shen <sup>1,2</sup>, Yaqun Liu <sup>1,2</sup>, Haibo Li <sup>1,2</sup> and Bo Liu<sup>1,2</sup>

<sup>1</sup>*Institute of Rock and Soil Mechanics, Chinese Academy of Sciences, Wuhan 430071, China*

<sup>2</sup>*University of Chinese Academy of Sciences, Beijing 100049, China*

Correspondence should be addressed to Yaqun Liu; [yqliu@whrsm.ac.cn](mailto:yqliu@whrsm.ac.cn)

Received 25 July 2023; Accepted 1 December 2023; Published 12 December 2023

Academic Editor: Zhuhua Tan

Copyright © 2023 Hui Shen et al. This is an open access article distributed under the Creative Commons Attribution License, which permits unrestricted use, distribution, and reproduction in any medium, provided the original work is properly cited.

The topography and the incident angle of seismic waves both have considerable effects on the seismic ground motions of canyons in a half-space. In this paper, the theory of wavefield decomposition and the artificial boundary is used to develop a method for inputting obliquely incident SV waves. Formulas for the equivalent nodal forces applied to the truncated boundary are derived and implemented in the finite element method. The validity of the proposed method is verified by a test case. A parametric study is then performed to investigate the influence of canyon geometry and incident angle of SV waves on the seismic response of trapezoidal canyons. The numerical results indicate that the canyon inclination has a more significant effect on the ground motion amplification than its height and width. The amplification effects are strongly related to the canyon inclination and the incident angle of SV waves. Additionally, the dominant frequency corresponding to the acceleration of the canyon crests is not sensitive to the incident angle of SV waves.

## 1. Introduction

Numerous postearthquake damage surveys [1–5] have shown that surface irregularities have a strong influence on ground motion during earthquakes, which is known as the topographic effect [6–9]. Canyons are common natural landforms in the mountainous region, and the topographic effect is important for the seismic design of structures located in the canyons, such as bridges across canyons and dams in valleys, where the peak ground accelerations vary significantly between the bottom of the canyon and the upper corners [10]. Although the consideration of topographic effects is recommended in several seismic codes [11], there are no design principles or regulations applicable to the seismic design of canyons in the current engineering practice. In this regard, it is necessary to further understand the influence of canyon topography on the topographic effects along the canyon surface.

Over the past decades, the topographic effects on the scattering and diffraction of seismic waves induced by the canyon topography have been extensively investigated in the

community of earthquake engineering. The analytical methods and the numerical methods are the two main methods used to study this problem. The problem of the scattering of antiplane waves (SH waves) in simple and smooth shapes of canyons, including semicircular canyons [12], semielliptical canyons [13], semiparabolic canyons [14], and U-shaped canyons [15], has received more attention in the analytical investigations due to the scalar form of the associated wave equation. The analytical solutions of the scattering of SH waves by a complicated canyon topography have received less attention due to the rapidly increasing difficulty in obtaining an analytical solution for it. In addition, the in-plane incident waves, such as longitudinal waves (P waves) or transverse waves (SV waves), cause mode conversion during the reflection of waves at the half-plane surface (Figure 1), so the analytical solution for the in-plane scattering by canyon is also very difficult to obtain. This has led to the application of various numerical methods to solve the problem of in-plane scattering induced by canyon topography, such as boundary methods [16], hybrid methods [17], and domain methods [18]. These numerical methods

can not only simulate the different incident conditions of P and SV waves but also study the more complex scattering of the in-plane waves by different shapes of canyons.

The seismic response of trapezoidal canyons has also been studied by many researchers. Based on the coupled finite and infinite element method, Zhao and Valliappan [19] studied the effects of the shape of the trapezoidal canyon on wave scattering due to the vertical incidence of P and SV waves. They reported that the canyon topography can have a dramatic effect on both the peak value and frequency content of the ground motion along the canyon surface during an earthquake and that a steeper canyon bank can induce a stronger wave mode conversion effect. Zhang et al. [20] proposed an analytical closed-form solution for the scattering of SH waves induced by a trapezoidal valley during earthquakes. Their results showed that the dynamic response at the ground surface is highly dependent on the steepness of the canyon and the incident angle of the excitations. Li et al. [21] developed a hybrid method to study a wave field while considering the effects of layered topography on the spatially variable motions through a symmetrical trapezoidal canyon in a layered half-space. They found that the surface motions of the trapezoidal canyon in the layered half-space are significantly different from those in the uniform case, and the layer conditions play important roles in determining the displacement amplitude along the canyon surface. Although much work has been done to date to study the wave scattering of trapezoidal canyons, the combined effect of trapezoidal canyon geometry and incident angle of SV waves on the topographic amplification and frequency-domain ground motions remains to be better understood. On the one hand, the significant influence of the incident angle on ground motion amplification has long been recognized [18, 22, 23]. Also, the oblique effect, formed by a combination of the direction of the incident wavefronts and the trapezoid bottom, can lead to apparent differences in peak ground accelerations at different locations on the canyon surface [10]. On the other hand, the detailed effects of the trapezoidal canyon geometries (e.g., the height of the canyon, the width of the canyon bottom, and the inclination of the canyon) on the amplification pattern of the ground motion require a further understanding, especially in the case of obliquely incident waves.

The main objective of this paper is to contribute to a better understanding of the effects of canyon topography and incident angle of SV waves on the seismic response of trapezoidal canyons through a parametric investigation. First, the input mechanisms of SV waves combined with an artificial boundary are introduced. Then, the numerical method for the incidence of vertical and oblique SV waves is implemented in the finite element (FE) method and verified by a test example. Subsequently, a parametric study is conducted to investigate the effects of the following factors on the topographic effect: (a) the normalized height of the canyon; (b) the normalized width of the canyon bottom; (c) the inclination of the canyon; and (d) the incident angle of SV waves. Four incident angles including one vertical incidence and three oblique incidences are considered in each numerical model. In addition, both amplification factors and

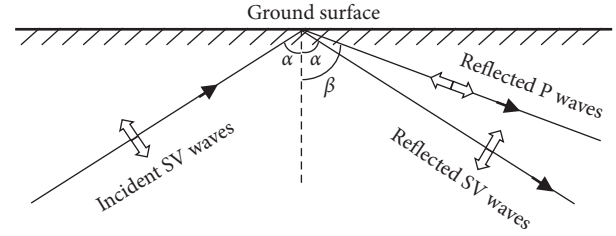


FIGURE 1: The mode conversion during the reflection of SV waves at the half-plane surface.

Fourier amplitude spectra along the canyon surface are obtained to reveal the seismic response of the canyon in time and frequency domains. Finally, the complexity of seismic wave interference in the trapezoidal canyon and the differences in numerical results are discussed.

## 2. Methodology

**2.1. Establishment of the Canyon Model.** Figure 2 shows a simplified model of a symmetrical trapezoidal canyon. The height of the canyon is  $h$ , the width of the canyon bottom is  $L$ , and the inclination of the canyon is  $i$ . The length of the upper flat ground surface behind both crests of the canyon, as well as the depth of the model, is at least three times the shear wavelength  $\lambda_s$ . The incident SV wave is assumed to propagate from the left side of the model at an angle of  $\theta_s$ . The incident angle  $\theta_s$  is defined as the angle between the direction of propagation of the SV wave and the vertical direction. Points A, D, and B, C are labeled to represent the crest and foot of the canyon, respectively. The  $y$ -axis of the coordinate system lies on the symmetry axis of the model, and the  $x$ -axis is parallel to the flat ground.

**2.2. Governing Equations.** Based on the decomposition of the wavefield, the total motion of the wave  $\mathbf{u}$  is composed of two parts: the motion of the scattering field  $\mathbf{u}^S$  and the free-field ground motion  $\mathbf{u}^F$ . Therefore, the total wavefield can be expressed as  $\mathbf{u} = \mathbf{u}^S + \mathbf{u}^F$ . On the truncated boundary, the equations of motion and the total motion of the wave at a given boundary node  $l$  can be expressed as follows:

$$m_l \ddot{u}_{li}^T + c_{linj} \dot{u}_{nj}^T + k_{linj} u_{nj}^T = f_{li}^S + f_{li}^F, \quad (1)$$

$$u_{li} = u_{li}^S + u_{li}^F, \quad (2)$$

where  $m_l$  is lumped mass of node  $l$ ,  $c_{linj}$  and  $k_{linj}$  represent the damping and stiffness coefficients, respectively;  $\dot{u}_{nj}^T$  and  $u_{nj}^T$  indicate the velocity and displacement of the boundary node  $n$ , respectively; and  $f_{li}^S$  and  $f_{li}^F$  are the loads in node  $l$  induced by the motion of the scattering field and the free-field motion, respectively. The subscripts  $i$  and  $j$  indicate components of the Cartesian coordinate, and  $i, j = 1, 2$  correspond to  $x, y$  in the two-dimensional problem.

The force of the boundary node corresponding to the motion of the scattering field is described as a function of the displacement and velocity fields:

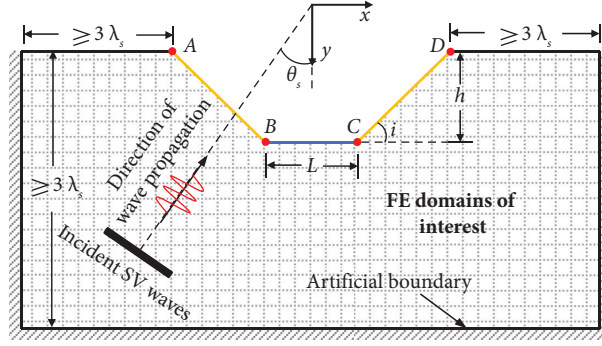


FIGURE 2: Numerical model of the trapezoidal canyon subjected to oblique incidence of SV waves.

$$f_{li}^S = (-K_{li}u_{li}^S - C_{li}\dot{u}_{li}^S)A_l, \quad (3)$$

where  $A_l$  represents the influence area of all elements around node  $l$  in the artificial boundary, and  $K_{li}$  and  $C_{li}$  are coefficients of the viscous-spring artificial boundary that are introduced in Section 2.3.

By substituting equations (2) and (3) into (1), we obtain the equation of motion at the boundary node  $l$ , that is,

$$m_l \ddot{u}_{li}^T + c_{linj} \dot{u}_{nj}^T + A_l C_{li} \dot{u}_{li}^T + k_{linj} u_{nj}^T + A_l K_{li} u_{li}^T = f_{li}^F + A_l K_{li} u_{li}^F + A_l C_{li} \dot{u}_{li}^F. \quad (4)$$

By combining the coefficients, equation (4) can be simplified as follows:

$$m_l \ddot{u}_{li}^T + (c_{linj} + \delta_{ln} \delta_{ij} A_l C_{li}) \dot{u}_{nj}^T + (k_{linj} + \delta_{ln} \delta_{ij} A_l K_{li}) u_{nj}^T = f_{li}^F + A_l K_{li} u_{li}^F + A_l C_{li} \dot{u}_{li}^F, \quad (5)$$

where  $\delta_{ij} = 1$  ( $i = j$ ),  $\delta_{ij} = 0$  ( $i \neq j$ ).

The right side of equation (5) shows the equivalent nodal force in artificial boundary nodes induced by free-field motion. By replacing the force term with the stress term on the right side of equation (5), the equivalent nodal force at  $l$  can be given as follows [24]:

$$f_{li} = (K_{li} u_{li}^F + C_{li} \dot{u}_{li}^F + \sigma_{li}^F) A_l. \quad (6)$$

It is clear from equation (6) that the motion of the incident wave can be converted into the equivalent nodal force applied to the corresponding artificial boundary nodes.

**2.3. The Viscous-Spring Artificial Boundary.** To eliminate the influence of wave reflection from the boundary, a viscous-spring artificial boundary is established by setting a series of springs and dashpots along the boundary [24], as shown in Figure 3. The elastic spring coefficient  $K$  and the damping coefficient  $C$  can be written as follows:

$$K_N = \frac{1}{1+A} \frac{\lambda + 2G}{2r}, \quad (7a)$$

$$C_N = B\rho c_p,$$

$$K_T = \frac{1}{1+A} \frac{G}{2r}, \quad (7b)$$

$$C_T = B\rho c_s,$$

where the superscripts  $N$  and  $T$  denote the normal and the tangential directions, respectively,  $A$  and  $B$  are the modified dimensionless coefficients, with suggested values of 0.8 and 1.1, respectively [24],  $\lambda$  is the Lamé constant,  $G$  is the shear modulus,  $r$  represents the distance between the source of the wave and the artificial boundary, and  $c_p = \sqrt{(\lambda + 2G)/\rho}$  and  $c_s = \sqrt{G/\rho}$  stand for the velocities of the compression wave and the shear wave in the medium, respectively.

**2.4. Equivalent Node Force for Obliquely Incident SV Waves.** As shown in Figure 4, the obliquely incident SV wave with angle  $\alpha$  decomposes into two parts when reaching the surface of the ground: one is the reflected SV wave with the

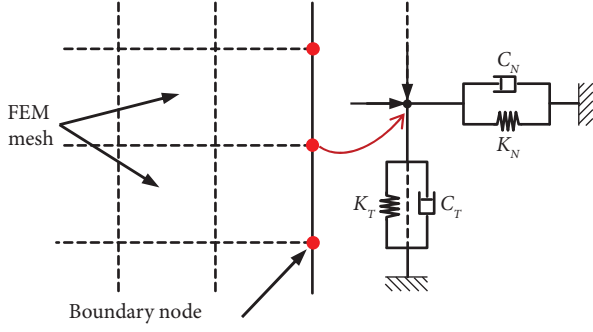


FIGURE 3: A sketch of the viscous-spring artificial boundary on the FE model.

same angle  $\alpha$ , and the other is the reflected  $P$  wave with angle  $\beta$ . The reflection angle  $\beta$  and the ratio of the amplitudes of the reflected wave and the incident wave can be expressed as follows:

$$\beta = \arcsin\left(\frac{c_p \sin \alpha}{c_s}\right), \quad (8a)$$

$$A_1 = \frac{c_s^2 \sin 2\alpha \sin 2\beta - c_p^2 \cos^2 2\alpha}{c_s^2 \sin 2\alpha \sin 2\beta + c_p^2 \cos^2 2\alpha}, \quad (8b)$$

$$A_2 = \frac{2c_p c_s \sin 2\alpha \cos 2\alpha}{c_s^2 \sin 2\alpha \sin 2\beta + c_p^2 \cos^2 2\alpha}, \quad (8c)$$

where  $A_1$  represents the ratio of the amplitude of the reflected SV wave to that of the incident SV wave, and  $A_2$  represents the ratio of the amplitude of the reflected  $P$  wave to that of the incident SV wave.

The length and the height of the truncated computational region are  $L_x$  and  $L_y$ , respectively (Figure 4). The total wave field at a given boundary node is a superposition of the incident SV waves, the reflected SV waves, and the reflected  $P$  waves. For a given boundary node  $l(x_0, y_0)$  in the free field, the displacement and stress on the left boundary are as follows [25]:

$$\begin{cases} u_{lx}^F = u_0(t - \Delta t_1) \cos \alpha - A_1 u_0(t - \Delta t_2) \cos \alpha + A_2 u_0(t - \Delta t_3) \sin \beta, \\ u_{ly}^F = -u_0(t - \Delta t_1) \sin \alpha - A_1 u_0(t - \Delta t_2) \sin \alpha - A_2 u_0(t - \Delta t_3) \cos \beta, \\ \sigma_{lx}^F = \frac{G}{c_s} \sin 2\alpha (\dot{u}_0(t - \Delta t_1) - A_1 \dot{u}_0(t - \Delta t_2)) + A_2 \frac{\lambda + 2G \sin^2 \beta}{c_p} \dot{u}_0(t - \Delta t_3), \\ \sigma_{ly}^F = \frac{G}{c_s} \cos 2\alpha (\dot{u}_0(t - \Delta t_1) + A_1 \dot{u}_0(t - \Delta t_2)) - A_2 \frac{G \sin 2\beta}{c_p} \dot{u}_0(t - \Delta t_3), \end{cases} \quad (9)$$

where the subscripts  $x$  and  $y$  represent the components of the waves,  $u_0(t)$  and  $\dot{u}_0(t)$  indicate the displacement-time history and velocity time history of the incident SV waves, respectively,  $A_1$  and  $A_2$  are amplitude ratios of the reflected

waves to the incident waves that are determined by equations (8b) and (8c), respectively, and  $\Delta t$  is the time lag in the propagation of incident waves from the wavefront at  $t = 0$  to the left boundary. It can be given as follows:

$$\begin{cases} \Delta t_1 = \frac{y_0 \cos \alpha}{c_s}, \\ \Delta t_2 = \frac{(2L_y - y_0) \cos \alpha}{c_s}, \\ \Delta t_3 = \frac{L_y - y_0}{c_p \cos \beta} + \frac{(L_y - (L_y - y_0) \tan \alpha \tan \beta) \cos \alpha}{c_s}. \end{cases} \quad (10)$$

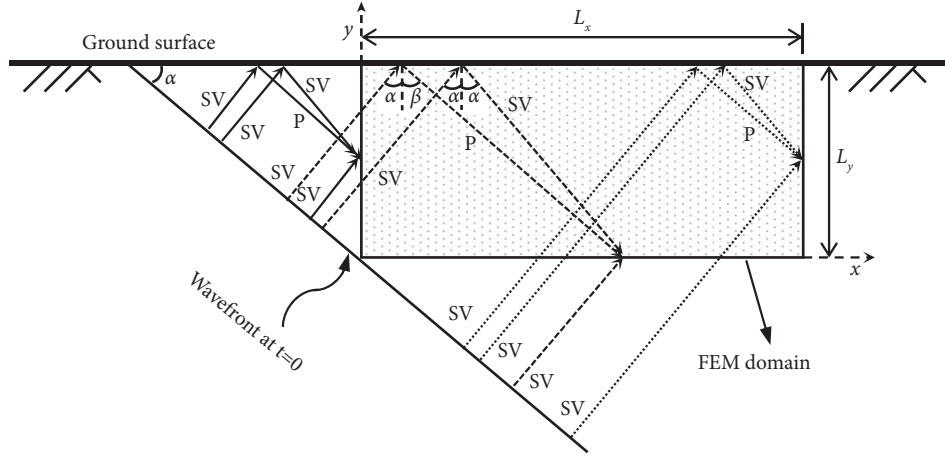


FIGURE 4: The incidence of SV wave in half-space and reflection on the ground surface.

The displacement and stress on the bottom boundary are as follows:

$$\begin{cases} u_{lx}^F = u_0(t - \Delta t_4)\cos\alpha - A_1 u_0(t - \Delta t_5)\cos\alpha + A_2 u_0(t - \Delta t_6)\sin\beta, \\ u_{ly}^F = -u_0(t - \Delta t_4)\sin\alpha - A_1 u_0(t - \Delta t_5)\sin\alpha - A_2 u_0(t - \Delta t_6)\cos\beta, \\ \sigma_{lx}^F = \frac{G}{c_s}\cos 2\alpha(\dot{u}_0(t - \Delta t_4) + A_1 \dot{u}_0(t - \Delta t_5)) - A_2 \frac{G\sin 2\beta}{c_p}\dot{u}_0(t - \Delta t_6), \\ \sigma_{ly}^F = \frac{G}{c_s}\sin 2\alpha(-\dot{u}_0(t - \Delta t_4) + A_1 \dot{u}_0(t - \Delta t_5)) + A_2 \frac{\lambda + 2G\cos^2\beta}{c_p}\dot{u}_0(t - \Delta t_6), \end{cases} \quad (11)$$

where the time lags of the propagation of incident waves from the wavefront at  $t = 0$  to the bottom boundary can be written as follows:

$$\begin{cases} \Delta t_4 = \frac{x_0 \sin\alpha}{c_s}, \\ \Delta t_5 = \frac{(2L_y + x_0 \tan\alpha)\cos\alpha}{c_s}, \\ \Delta t_6 = \frac{L_y}{c_p \cos\beta} + \frac{(L_y \cos\alpha + x_0 \sin\alpha - L_y \tan\beta \sin\alpha)}{c_s}. \end{cases} \quad (12)$$

The formulas describing the displacement on the right boundary are the same as those on the left boundary, but an additional time  $L_x \sin\alpha / c_p$  needs to be added to  $\Delta t_1$ ,  $\Delta t_2$ , and  $\Delta t_3$  owing to the additional distance  $L_x$  traveled by the wave. The stresses on the right boundary are the same as those on the left boundary but in the opposite direction.

**2.5. Verification.** In this section, a test case is considered to assess the overall accuracy of the presented numerical methodology, which involves the propagation of in-plane SV waves in a homogeneous elastic half-space with an oblique incident angle. Figure 5(a) shows a truncated region used to simulate the propagation of obliquely incident SV waves in

a semi-infinite space. The region is assumed to be an elastic homogeneous medium with Young's modulus  $E = 6 \text{ Ga}$ , mass density  $\rho = 2450 \text{ kg/m}^3$ , and Poisson's ratio  $\nu = 0.3$ . The corresponding velocities of the shear wave  $c_s$  and the compression wave  $c_p$  are  $971 \text{ m/s}$  and  $1816 \text{ m/s}$ , respectively.

The size of the computational domain is  $2000 \text{ m} \times 1000 \text{ m}$ , and the incident angle is  $\theta_s = 20^\circ$ . An impulse wave with an amplitude of  $1 \text{ m}$  and an acting time of  $0.3 \text{ s}$  is used as the incident SV wave, as shown in Figure 5(b). The corresponding definition of the incident wave is given as follows:

$$P(\tau) = 16P_0 \left[ G(\tau) - 4G\left(\tau - \frac{1}{4}\right) + 6G\left(\tau - \frac{1}{2}\right) - 4G\left(\tau - \frac{3}{4}\right) + G(\tau - 1) \right], \quad (13a)$$

$$G(\tau) = \tau^3 H(\tau), \quad (13b)$$

$$\tau = \frac{t}{T},$$

where  $t$  denotes time,  $H(\tau)$  is the Heaviside function,  $P_0$  is the amplitude of the impulse, and  $P_0 = 1.0 \text{ m}$ . Herein,  $T$  is the acting time of the impulse, and  $T = 0.3 \text{ s}$ .

Figure 6 shows the contours of the displacement magnitude at different arrival times of the obliquely incident SV waves. The figure clearly shows the propagation and reflection of the incident wave, which means that the propagation of SV waves in the semi-infinite space has been effectively simulated without wave reflection along the artificial boundary. To verify the accuracy of the input method, two reference points  $A$  (1000, 1000) and  $B$  (1000, 500), labeled in Figure 5, are selected to monitor the displacement components in the  $x$ - and  $y$ -directions (denoted by  $U_x$  and  $U_y$ , respectively). A comparison of the displacement-time histories between the theoretical solution and the numerical results at points  $A$  and  $B$  is shown in Figure 7. It is clearly shown that the numerical results are in good agreement with the results of the theoretical solution, indicating that the introduced input method is appropriate for simulating obliquely incident SV waves.

### 3. Description of the Parameters

The variations in the topography of the canyon ( $h$ ,  $L$ , and  $i$ ) are shown in Figure 8. The incident angle  $\theta_s$  varies from  $0^\circ$  to  $30^\circ$  in increments of  $10^\circ$  for each numerical model. The Ricker wavelets are used as the incident SV waves since they are commonly used as idealized input seismograms (Figure 9). The acceleration time history of the Ricker wave is defined as follows:

$$r(t) = \left(1 - 2\pi^2 f_c^2 (t - t_0)^2\right) e^{-\pi^2 f_c^2 (t - t_0)^2}, \quad (14)$$

where  $f_c$  and  $t_0$  represent the central frequency of the Fourier spectrum and the time when the acceleration reached its peak, respectively. A Ricker wavelet with an amplitude of  $1 \text{ m/s}^2$  and a central frequency of  $4 \text{ Hz}$  is selected as the incident wave.

A homogeneous elastic medium with mass density  $\rho = 2650 \text{ kg/m}^3$ , elastic modulus  $E = 20 \text{ Ga}$ , and Poisson's ratio  $\nu = 0.25$  is used to represent the rock material in the numerical model. We also introduce dimensionless frequency for normalizing the height of the canyon and the width of its bottom; therefore, the geometric parameters  $h$

and  $L$  are both normalized by the shear wavelength  $\lambda_s$  in this study:

$$\eta_h = \frac{h}{\lambda_s}, \quad (15)$$

$$\eta_L = \frac{L}{\lambda_s}.$$

In summary, this study mainly considered variations in the following parameters:

- (1) The angle of incidence:  $\theta_s$  varies from  $0^\circ$  to  $30^\circ$  for the incidence of SV waves in increments of  $10^\circ$
- (2) Normalized height of the canyon:  $\eta_h$  varies from 0.5 to 2.0, in increments of 0.5
- (3) Normalized width of the canyon bottom:  $\eta_L$  varies from 0.5 to 2.0, in increments of 0.5
- (4) The inclination of the canyon:  $i$  varies from  $15^\circ$  to  $60^\circ$ , in increments of  $15^\circ$

### 4. Results

*4.1. Effects of the Normalized Height of the Canyon.* Figure 10 compares the acceleration amplification along the canyon surface for vertically and obliquely incident SV waves with  $\eta_h$  varying from 0.5 to 2.0. Note that the horizontal coordinates of the ground surface are normalized by the shear wavelength ( $\lambda_s$ ) in each subplot, and the amplification factor curves are plotted in both the three-dimensional perspective view and the corresponding two-dimensional front view to better illustrate the variation of amplification factors. The vertical solid lines in the subplots represent the location of the left and right canyon crests while the vertical dashed lines represent the location of the foot of the canyon. The horizontal and vertical amplification factors (HAF and VAF) are defined as the ratio of the maximum horizontal and vertical ground accelerations measured at the surface to the maximum horizontal acceleration in the far field, respectively.

$$\text{HAF} = \frac{a_{h,\max}}{a_{\text{ff},\max}}, \quad (16)$$

$$\text{VAF} = \frac{a_{v,\max}}{a_{\text{ff},\max}}$$

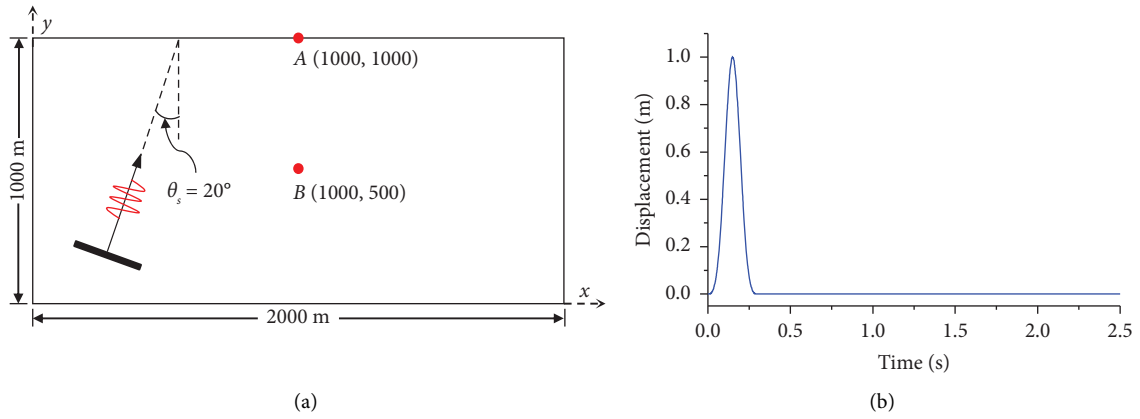


FIGURE 5: (a) A sketch of obliquely incident SV wave in half-space and (b) the input seismic motion.

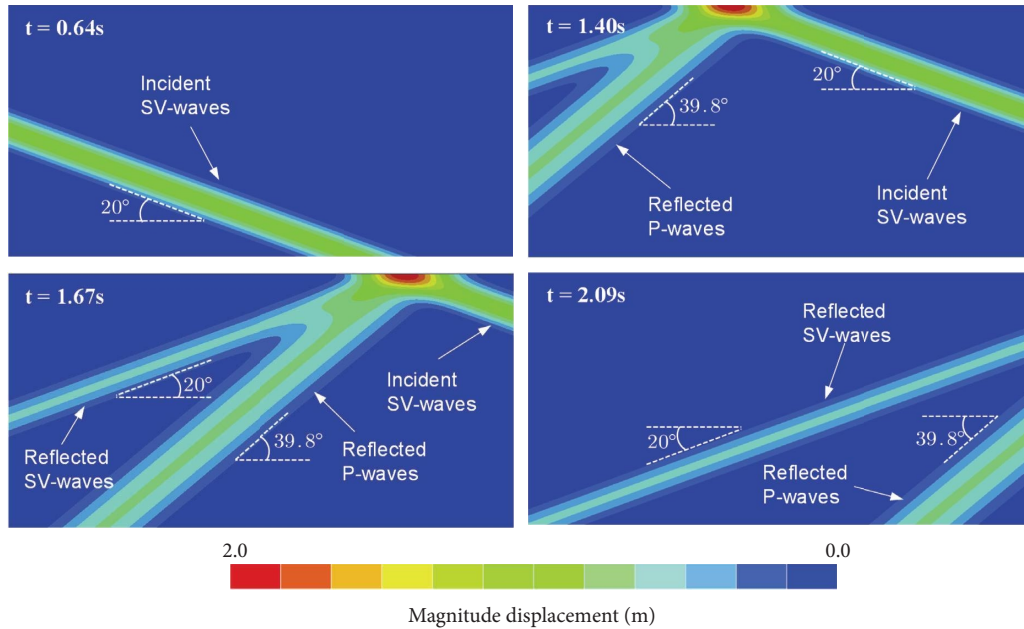


FIGURE 6: Displacement contours of SV wave propagated in semi-infinite space.

As shown in Figure 10(a), the horizontal amplification factors (HAF) fluctuate strongly along the canyon surface, alternating between amplification (i.e.,  $HAF > 1.0$ ) and deamplification (i.e.,  $HAF < 1.0$ ). The results associated with the HAF in Figure 10(a) reveal the following findings. (1) The curves of the HAF are almost symmetrically distributed along the canyon surface due to the symmetrical shape of the trapezoidal canyon when  $\theta_s = 0^\circ$ , while the curves of the HAF become unsymmetrical when  $\theta_s > 0^\circ$ . (2) The horizontal amplification of the ground motion is pronounced around the canyon crests in both cases of vertical incidence and oblique incidence. (3) For vertical incidence, the HAF in the vicinity of the canyon crests shows an increasing trend with the increasing normalized canyon height ( $\eta_h$ ). (4) It is also observed that the amplification patterns are highly dependent on the incident angle of SV waves for oblique incidence. Specifically, the HAF around the right crest of the

canyon is significantly larger than that around the left crest when  $\theta_s = 10^\circ$ , and the peak values of the HAF increase with increasing  $\eta_h$ . However, in the case of  $\theta_s \geq 20^\circ$ , the pronounced amplification appears on the left side of the canyon, and the right side of the canyon is nearly deamplified, which is opposite to the amplification pattern at  $\theta_s = 10^\circ$ . This indicates that the interference of the wave fields on the right side of the canyon is significantly affected by a larger  $\theta_s$  (such as  $30^\circ$ ), which in turn leads to a change in the amplification pattern.

The results associated with the VAF in Figure 10(b) reveal that the overall vertical amplification under oblique incidence ( $\theta_s > 0^\circ$ ) is obviously greater than that under vertical incidence ( $\theta_s = 10^\circ$ ). In the case of oblique incidence, the vertical amplification on the right side of the canyon is predominant compared to that on the left side of the canyon, which means that the reflected P waves and generated

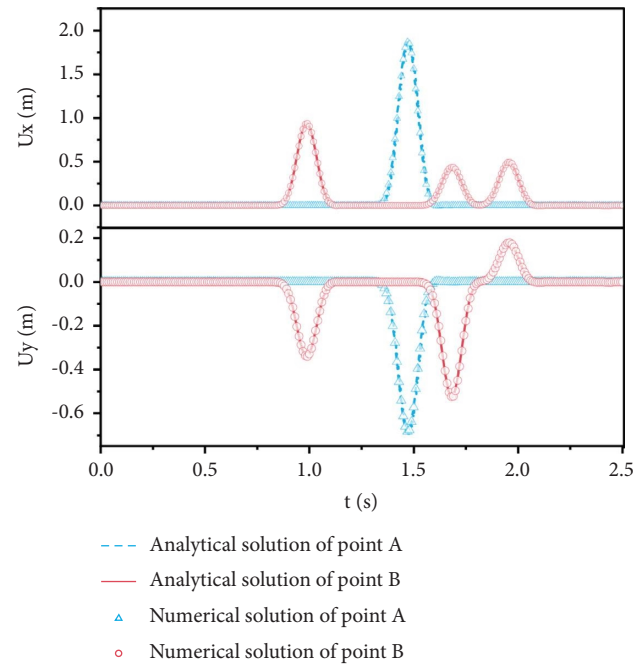


FIGURE 7: Comparison of displacement-time histories between theoretical solution and numerical results at monitoring points A and B.

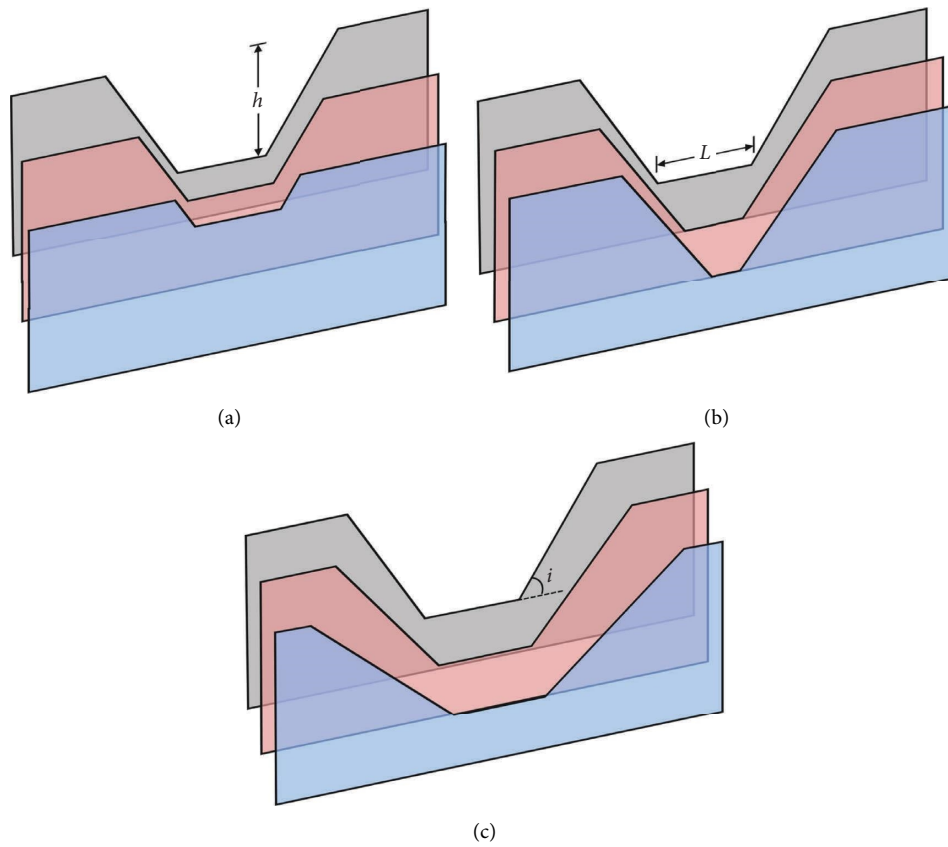


FIGURE 8: The schematic diagram of various canyon geometries, including variations in (a) the height of the canyon, (b) the width of the canyon bottom, and (c) the inclination of the canyon.

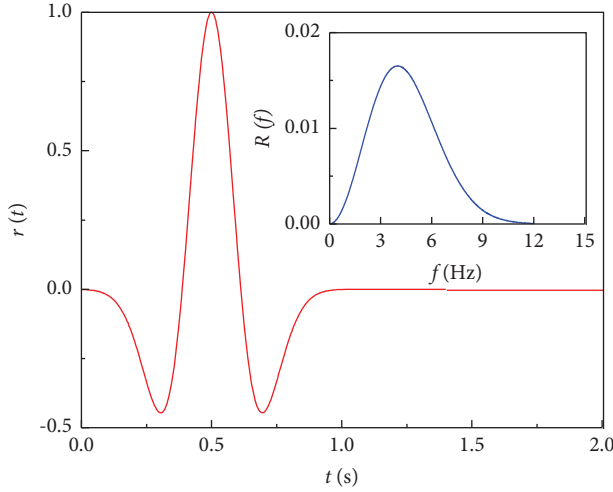


FIGURE 9: The acceleration time history of the incident Ricker wavelet ( $f_c = 4$  Hz and  $t_0 = 0.5$  s) and the corresponding Fourier amplitude spectrum.

surface waves on the right side of the canyon resulted in a relatively stronger vertical ground motion. The maximum value of the VAF is more likely to appear in the vicinity of the canyon crests when  $\theta_s \leq 10^\circ$ , which is similar to the horizontal amplification as shown in Figure 10(a) while the maximum vertical amplification occurs at about one shear wavelength ( $\lambda_s$ ) from the right foot of the canyon when  $\theta_s \geq 20^\circ$  for both shallower canyon (e.g.,  $\eta_h = 0.5$ ) and deeper canyon (e.g.,  $\eta_h = 2.0$ ). In addition, for a given  $\theta_s$  ( $\theta_s \geq 20^\circ$ ), the maximum value of VAF ( $\text{VAF}_{\max}$ ) remains almost constant under different  $\eta_h$  (e.g.,  $\text{VAF}_{\max} = 0.6$  for  $\theta_s = 20^\circ$  and  $\text{VAF}_{\max} = 0.8$  for  $\theta_s = 30^\circ$ ).

By applying the fast Fourier transform (FFT) to the recorded ground accelerations, the Fourier amplitude spectra of surface ground motions are obtained. The magnitude of the ground motion in a given frequency component can be represented by the corresponding Fourier amplitude. Contours of the Fourier amplitude spectrum for horizontal and vertical accelerations along the canyon surface at different values of  $\eta_h$  and  $\theta_s$  are given in Figure 11. The white solid lines and dashed lines in each subplot represent the crest and the foot of the canyon, respectively. It is clearly shown that the Fourier amplitude is mainly distributed in the range of 1–8 Hz, which corresponds to the width of the frequency band of the incident Ricker wave. As expected, the pronounced ground response is concentrated in the frequency range of 3–5 Hz, where most of the energy is carried by the incident waves. In the horizontal direction, the Fourier amplitudes near and behind the crests of a deeper canyon ( $\eta_h = 2.0$ ) are greater than those of a shallower canyon ( $\eta_h = 0.5$ ) for vertically incident waves ( $\theta_s = 0^\circ$ ), while the Fourier amplitudes behind the right crest of a shallower canyon are greater than that of a deeper canyon for obliquely incident waves ( $\theta_s = 30^\circ$ ). In the vertical direction, the Fourier amplitudes under obliquely incident waves are significantly larger than those under vertically incident waves, indicating a strong oblique effect of the incident waves. In addition, the vertical Fourier amplitudes

behind the right crest of a shallower canyon are also larger than those of a deeper canyon under oblique incidence, which is similar to that in the horizontal direction.

Figure 12 clearly shows the distribution of the Fourier amplitude at the left and right canyon crests in the frequency domain for different  $\eta_h$  and  $\theta_s$ . The vertical dashed lines in each subplot indicate the central frequency (4 Hz) of the incident Ricker wavelet. In the horizontal direction (Figure 12(a)), the results reveal the following findings. (1) The frequency corresponding to the peak Fourier amplitude (PFA) at the left and right canyon crests is close to the central frequency of the incident wave. (2) The PFA at the left canyon crest does not change significantly with the increase of the incident angle  $\theta_s$ , regardless of  $\eta_h = 0.5$  or  $\eta_h = 2.0$ , while the PFA at the right canyon crest decreases rapidly with the increase of the incident angle  $\theta_s$ . In the vertical direction (Figure 12(b)), the results reveal the following findings. (1) The frequency corresponding to the PFA at the canyon crests varies between 3 Hz and 5 Hz. (2) For a shallower canyon ( $\eta_h = 0.5$ ), the PFA increases with increasing incident angle  $\theta_s$ , especially at the right canyon crest. The difference between the PFA at the left and right canyon crests is obvious at  $\theta_s = 30^\circ$ . (3) For a deeper canyon ( $\eta_h = 2.0$ ), the difference between the PFA on the left and right canyon crests is apparent at  $\theta_s = 10^\circ - 20^\circ$ .

**4.2. Effects of Normalized Width of the Canyon Bottom.** HAF and VAF curves for different values of  $\eta_L$  from 0.5 to 2.0 are shown in Figure 13. For a given  $\theta_s$ , the horizontal amplification curves for different  $\eta_L$  have similar shapes. In all cases except  $\eta_L = 1.0$ , the maximum values of HAF near the canyon crests are almost the same for a given incident angle  $\theta_s$  despite the increasing  $\eta_L$ . In addition, the vertical amplification curves for different  $\eta_L$  also have similar shapes for a given  $\theta_s$ . The vertical amplification generally increases with increasing  $\theta_s$  for a given  $\eta_L$ . For both horizontal and vertical amplifications, the shapes of the amplification factor curves at different  $\eta_L$  are similar for the same incident angle  $\theta_s$ , and no significant differences in the maximum amplification are observed for a given  $\theta_s$ , implying that the width of the canyon bottom has little effect on the seismic response of the canyon.

Figure 14 shows plots of the contours of the Fourier amplitude in the case of horizontal and vertical ground accelerations at different values of  $\eta_L$  and  $\theta_s$ . For a given incident angle  $\theta_s$ , the variation of  $\eta_L$  has no significant effect on the horizontal and vertical Fourier amplitude spectra. Therefore, similar conclusions can be drawn as in the previous section.

**4.3. Effects of Inclination of the Canyon.** The variation of horizontal and vertical amplifications versus the inclination of the canyon for different incident angles of SV waves is plotted in Figure 15. The results associated with the HAF in Figure 15(a) reveal the following findings. (1) The shape of the HAF curves is mainly dependent on the inclination of the canyon. (2) A mode conversion of the horizontal amplification pattern is observed with an increasing incident

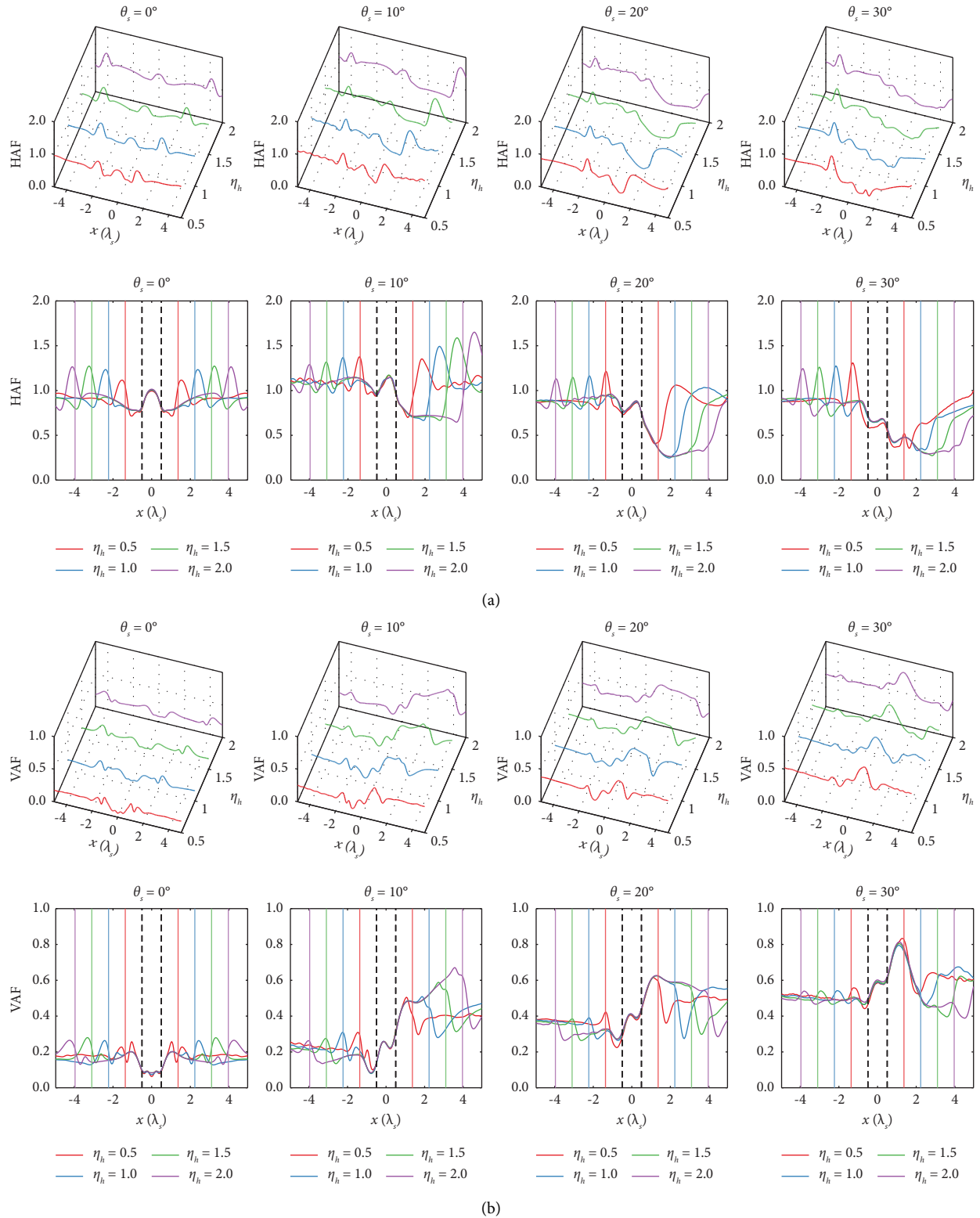


FIGURE 10: Effects of normalized canyon height  $\eta_h$  on the (a) horizontal and (b) vertical acceleration amplifications with  $\eta_L = 1.0$  and  $i = 30^\circ$  under incident angles  $\theta_s$  of  $0^\circ$ ,  $10^\circ$ ,  $20^\circ$ , and  $30^\circ$ . The vertical solid lines in the subplots represent the location of the left and right canyon crests while the vertical dashed lines indicate the positions of the canyon feet.

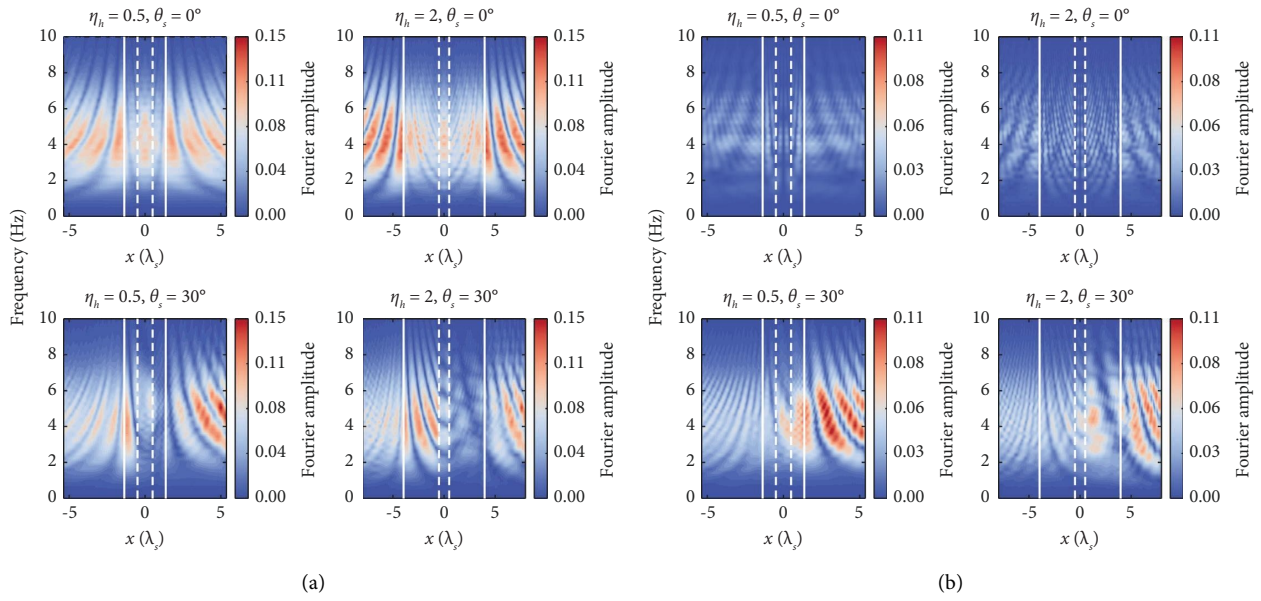


FIGURE 11: Effect of normalized canyon height  $\eta_h$  on the Fourier amplitude spectrum of (a) horizontal and (b) vertical ground accelerations for configurations with  $\eta_L = 1.0$  and  $i = 30^\circ$  under vertically and obliquely incident SV waves. The white solid lines and dashed lines represent the locations of the crests and feet of the canyon model, respectively.

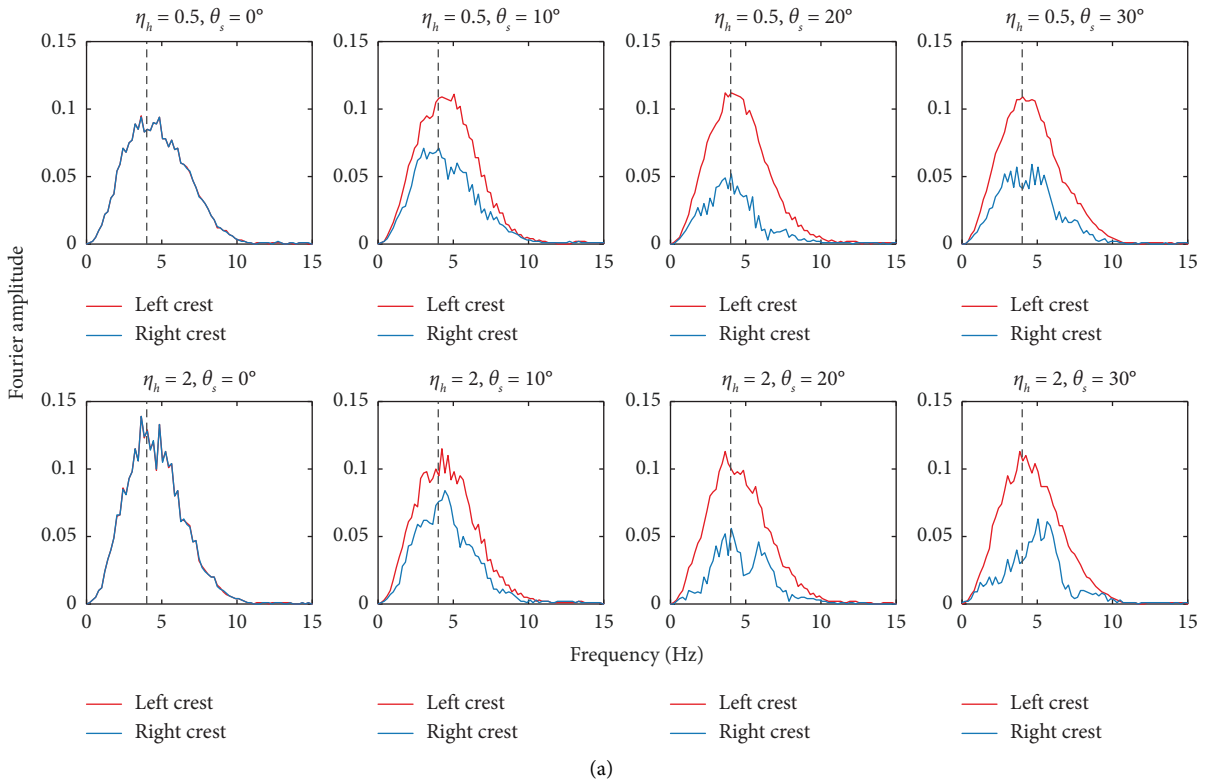


FIGURE 12: Continued.

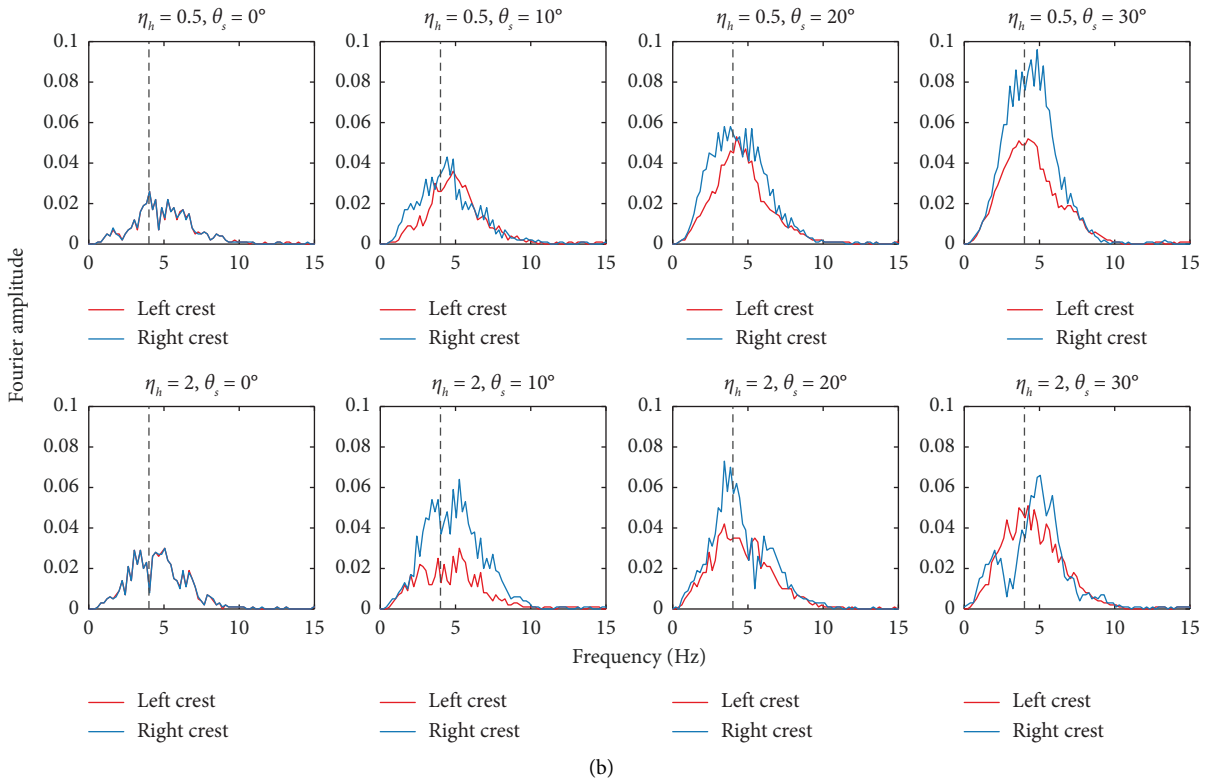


FIGURE 12: The (a) horizontal and (b) vertical Fourier amplitudes at the canyon crests for different heights of the canyon and incident angles of SV waves.

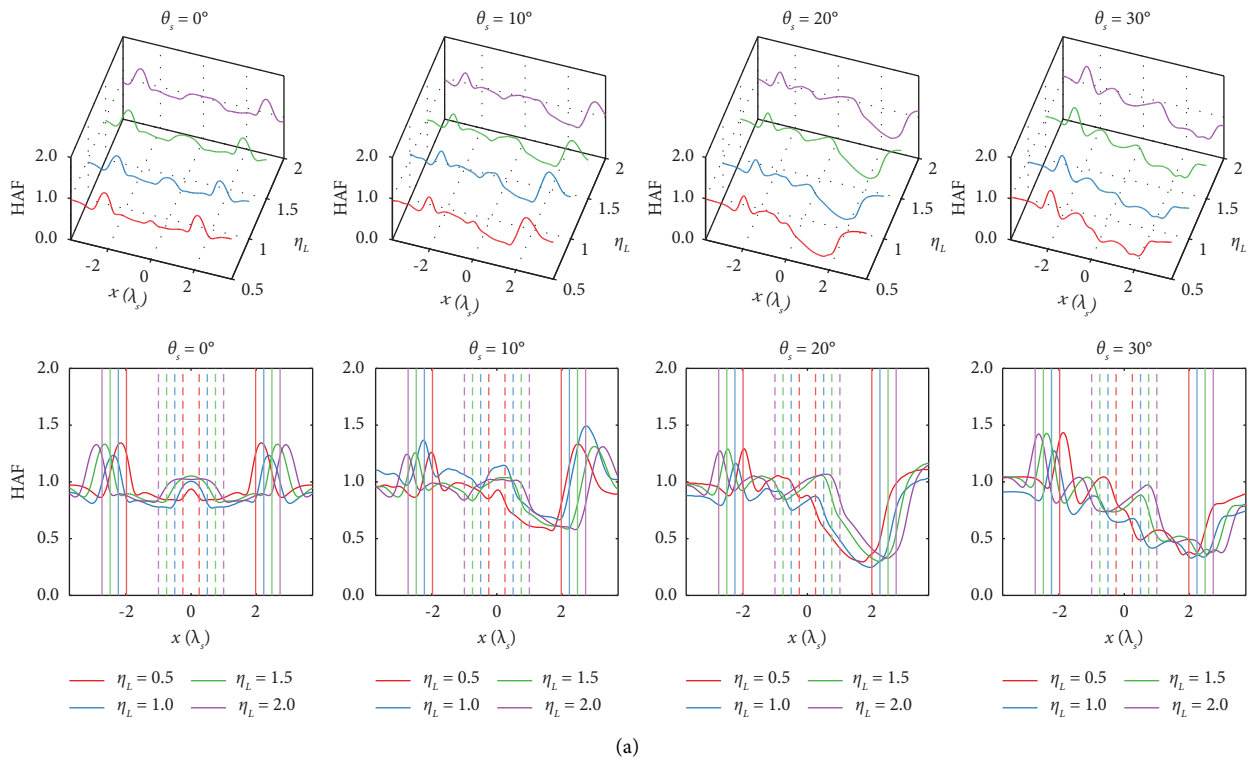


FIGURE 13: Continued.

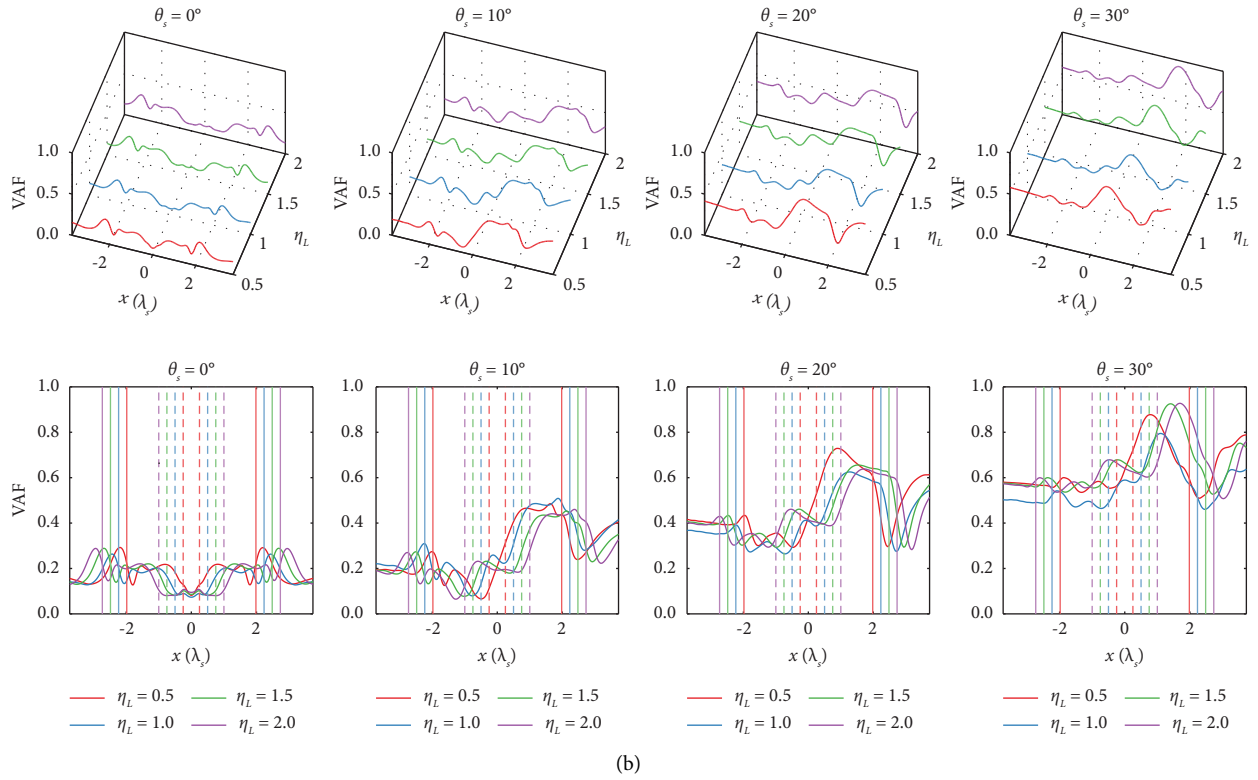


FIGURE 13: Effects of normalized width of the canyon bottom  $\eta_L$  on the (a) horizontal and (b) vertical acceleration amplifications with  $\eta_h = 1.0$  and  $i = 30^\circ$  under incident angles  $\theta_s$  of  $0^\circ$ ,  $10^\circ$ ,  $20^\circ$ , and  $30^\circ$ . The vertical solid lines in the subplots represent the location of the left and right canyon crests while the vertical dashed lines indicate the positions of the canyon feet.

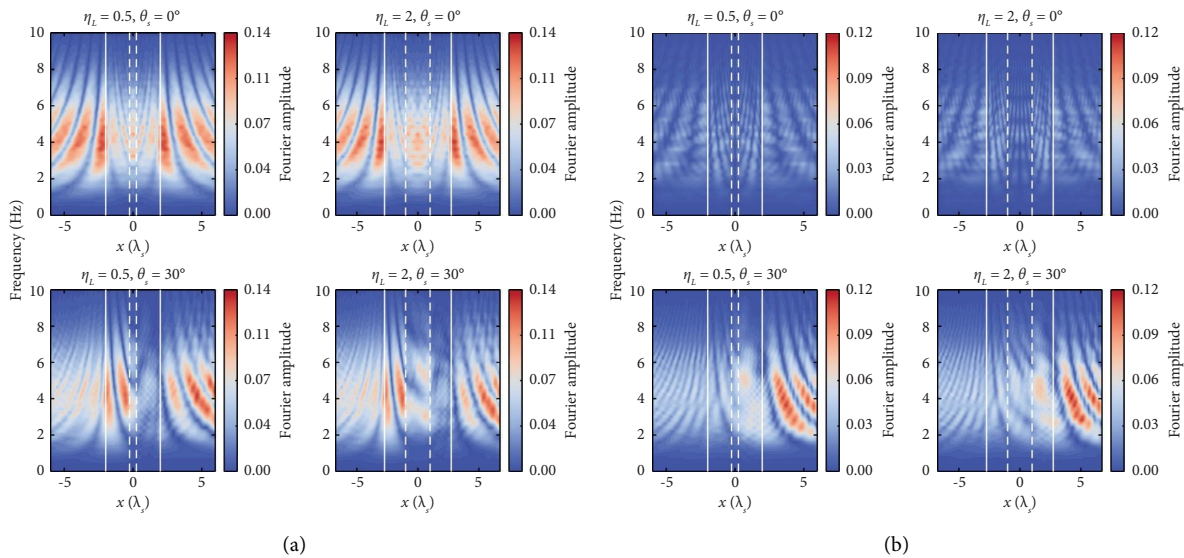


FIGURE 14: Effect of normalized canyon height  $\eta_L$  on the Fourier amplitude spectrum of (a) horizontal and (b) vertical ground accelerations for configurations with  $\eta_h = 1.0$  and  $i = 30^\circ$  under vertically and obliquely incident SV waves. The white solid lines and dashed lines represent the locations of the crests and feet of the canyon model, respectively.

angle  $\theta_s$ , (3) The incident angle of SV waves has a significant influence on the horizontal amplification, especially for a steeper canyon (e.g.,  $i = 45^\circ$  or  $60^\circ$ ). For example, the HAF at the left canyon crest is about 1.0 for  $i = 60^\circ$  and  $\theta_s = 0^\circ$ ,

while the HAF increases significantly to 1.6 for  $i = 60^\circ$  and  $\theta_s = 30^\circ$ . (4) The peak values of HAF at the canyon bottom are almost the same for a given  $\theta_s$ , which is not related to the inclination of the canyon. The results associated with the

VAF in Figure 15(b) reveal the following findings. (1) For a given  $\theta_s$ , the maximum VAF increases with increasing inclination of the canyon. (2) As the  $\theta_s$  increases, the difference in VAF between different inclinations of the canyon gradually decreases.

Figures 16(a) and 16(b) show the variation of Fourier amplitude spectra with different  $i$  and  $\theta_s$  in the horizontal and vertical directions, respectively. In the case of vertical incidence ( $\theta_s = 0^\circ$ ), the magnitude of the horizontal ground motion was almost uniformly distributed over the entire canyon surface for  $i = 15^\circ$ . As the canyon inclination increases, the pronounced horizontal ground motions are concentrated near or behind the canyon crest. It is also clear that the vertical ground motions are significantly enhanced with increasing canyon inclination, and the pronounced surface motions gradually converge at the crests. In the case of obliquely incident waves ( $\theta_s = 30^\circ$ ), the intensity of ground motions behind the right crest decreases in both horizontal and vertical directions with increasing canyon inclination. While the horizontal and vertical ground motions on the left side of the canyon are enhanced with increasing inclination. The distribution of the Fourier spectrum becomes more complex with increasing inclination, indicating that the inclination of the canyon has a significant effect on the seismic ground motions of the canyon.

The horizontal and vertical Fourier amplitudes at the left and right canyon crests for different  $i$  and  $\theta_s$  are shown in Figure 17. In the horizontal direction, for a gentler canyon (e.g.,  $i = 15^\circ$ ), the difference in PFA between the left and right canyon crests becomes apparent when the incident angle of SV waves is larger (e.g.,  $\theta_s = 30^\circ$ ), while the difference in PFA between the left and right canyon crests for a steeper canyon (e.g.,  $i = 60^\circ$ ) is not obvious under different  $\theta_s$ . In the vertical direction, the PFA at the left and right canyon crests increases with increasing incident angle  $\theta_s$  for a gentler canyon (e.g.,  $i = 15^\circ$ ). However, for a steeper canyon (e.g.,  $i = 60^\circ$ ), the PFA at the left crest decreases and then increases with increasing incident angle  $\theta_s$ , and the PFA at the right crest increases and then decreases with increasing incident angle  $\theta_s$ . It is also observed that for oblique incidence, in some cases, the frequencies corresponding to the PFA at the left and right crests of a steeper canyon are distributed on either side of the incident wave frequency (i.e., 4 Hz). For example, in the case of  $i = 60^\circ$  and  $\theta_s = 20^\circ$  for the horizontal direction, and the cases of  $i = 60^\circ$  and  $\theta_s = 30^\circ$  for the vertical direction. In summary, the frequency corresponding to the PFA in the horizontal and vertical directions is in the range of 3–5 Hz, which is close to the incident wave frequency.

## 5. Discussion

This study investigates the effects of the canyon geometry and incident angle of SV waves on the seismic response of trapezoidal canyons. The incident angle of SV waves and the inclination of the canyon play important roles in the seismic ground motions of the canyons. For a given incident angle  $\theta_s$ , the amplification factor curves for similar topographic

geometries (e.g., the dimensionless height  $h/\lambda_s$  or dimensionless width  $L/\lambda_s$ ) have similar shapes, which means that they result from similar patterns of the waveform [26]. However, the inclination of the canyon shows a more significant influence on the seismic amplification of the canyon than the other two canyon geometry parameters. Figure 18 shows the seismogram synthetics of the horizontal and vertical ground motion components, which include the following waveforms: (1) direct SV waves (denoted by SV), (2) reflected  $P$  waves (denoted by  $P$ ), and (3) diffracted Rayleigh waves generated by sharp corners (denoted by  $R_1$  and  $R_2$ ). It is clearly shown that the sharper corners significantly distort the seismic waves. This may be attributed to the sharper corners that a steeper canyon has compared to a flatter canyon, leading to strong scattering waves. Meanwhile, a stronger effect of mode conversion of the waves is induced by a larger incident angle  $\theta_s$ , indicating that the intensity of seismic ground motions may be underestimated if the oblique incidence of the seismic wave is ignored. In addition, it is found that the canyon surface is subjected to stronger horizontal ground motion than its vertical motion.

The amplification patterns and seismic ground motions under different incident conditions can be explained by further analysis of the canyon wavefields. The snapshots of the acceleration wave field and the contours of the absolute acceleration amplitude for different canyon configurations are shown in Figures 19 and 20. As shown in Figure 19, two canyon models with different normalized heights ( $\eta_h = 0.5$  in Figures 19(a) and  $\eta_h = 2$  in 19(b)) are subjected to the obliquely incident wave ( $\theta_s = 20^\circ$ ). It can be seen that the interference between the reflected waves from the horizontal ground surface and the scattering waves from the canyon surface is mainly concentrated on the left part of the canyon, i.e., the side of the incident wave. Hence, the wavefields on the left side are more complicated than those on the right side, which can be explained by the ‘‘canyon-decay effect.’’ The total internal wavefields are similar for both shallower and deeper canyons despite their different heights. However, a deeper canyon may show a more pronounced ‘‘canyon-decay effect’’ compared to a shallower canyon since the complicated wavefields after interference are blocked by the left side of the deeper canyon, and thus the incident waves traveling to the right side of the canyon are less affected. Although the incident SV waves mainly influence the horizontal ground motions of the canyon surface, they also cause ground motions in the vertical direction (see Figure 18(b)). The vertical ground motions are mainly induced by the reflected  $P$  waves and Rayleigh waves which are less affected on the right side of the canyon, hence the vertical ground motions on the right side of the canyon are stronger than those on the left side of the canyon. On the other hand, the reflected  $P$  waves on the left side of the canyon interfere with the scattered waves, and the resulting vertical ground motions will be further reduced. For canyons with different inclinations (shown in Figure 20), the degree of complexity of the wavefields becomes different. A more complex interference between the reflected waves and the scattering waves is observed for a canyon with a steeper

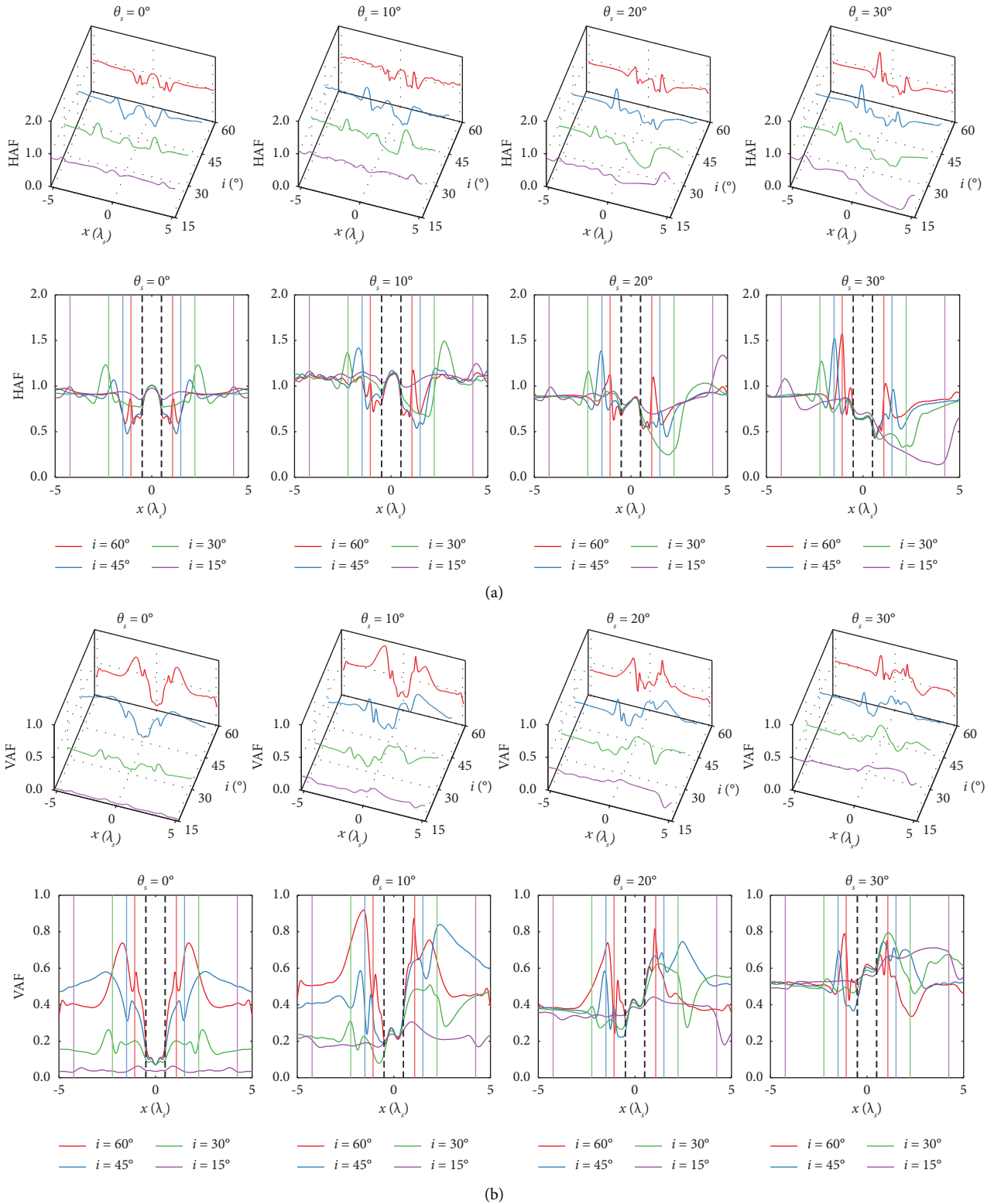


FIGURE 15: Effects of canyon inclination  $i$  on the (a) horizontal and (b) vertical acceleration amplifications with  $\eta_h = 1.0$  and  $\eta_L = 1.0$  under incident angles  $\theta_s$  of  $0^\circ$ ,  $10^\circ$ ,  $20^\circ$ , and  $30^\circ$ . The vertical solid lines in the subplots represent the location of the left and right canyon crests while the vertical dashed lines indicate the positions of the canyon feet.

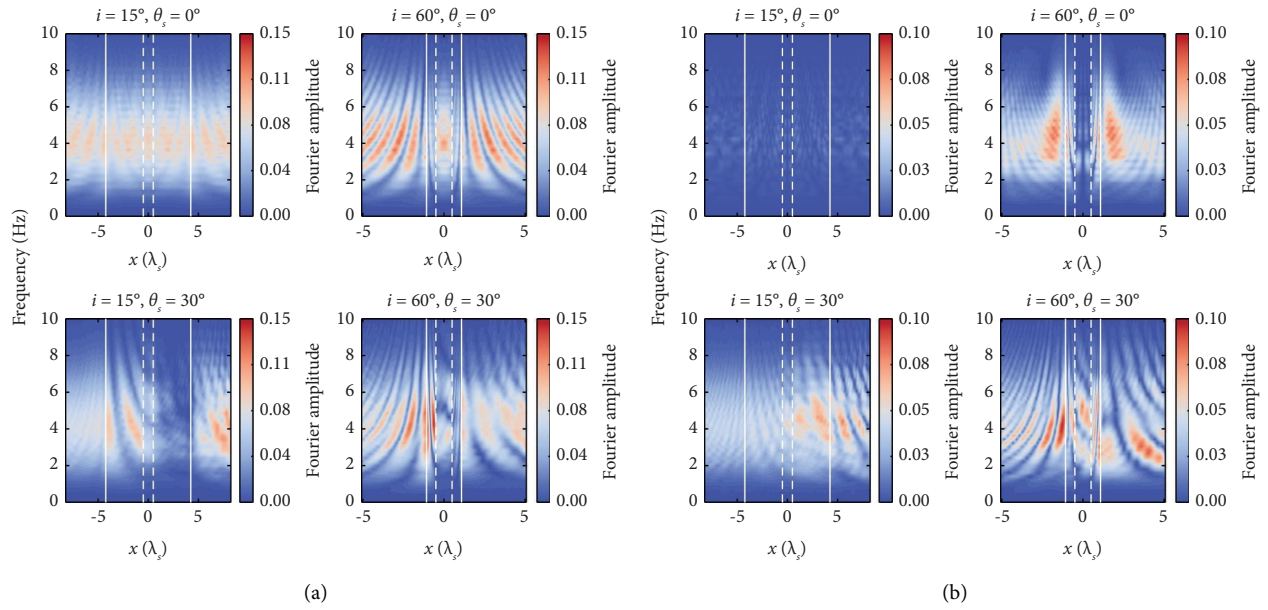


FIGURE 16: Effect of the inclination of the canyon  $i$  on the Fourier amplitude spectrum of (a) horizontal and (b) vertical ground accelerations for configurations with  $\eta_h = 1.0$  and  $\eta_L = 1.0$  under vertically and obliquely incident SV waves. The white solid lines and dashed lines represent the locations of the crests and feet of the canyon model, respectively.

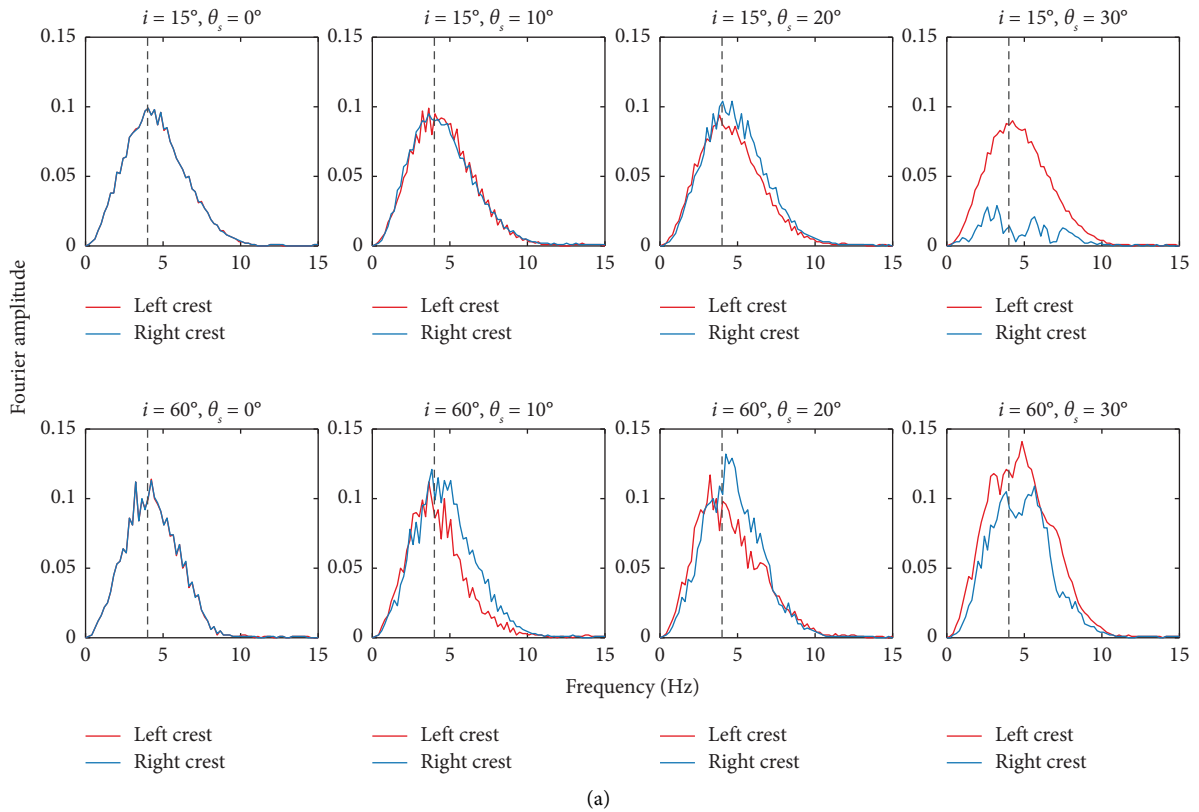


FIGURE 17: Continued.

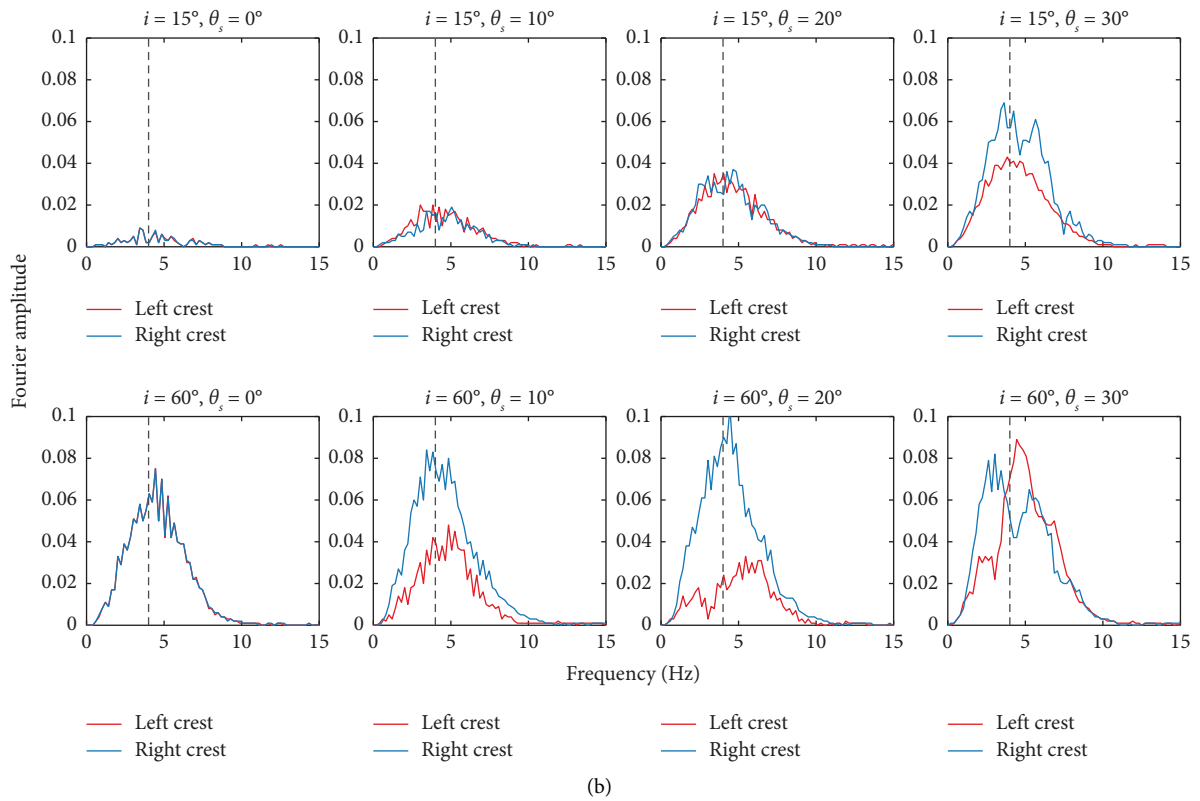


FIGURE 17: The (a) horizontal and (b) vertical Fourier amplitudes at the canyon crests for different inclinations of the canyon and incident angles of SV waves.

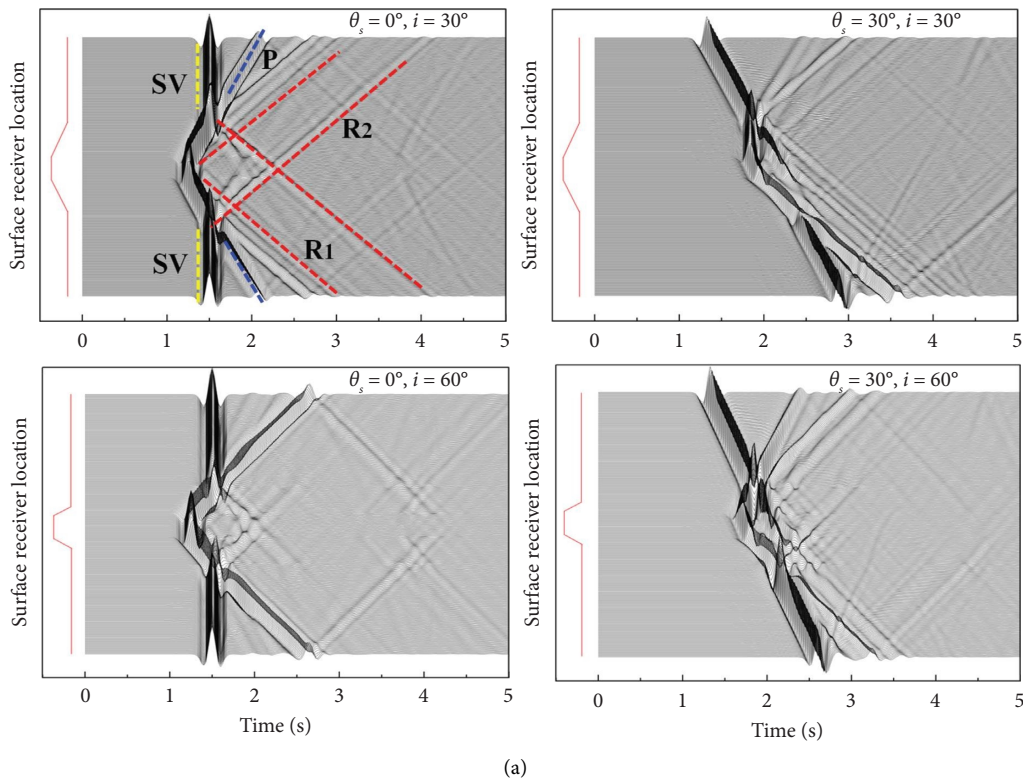


FIGURE 18: Continued.

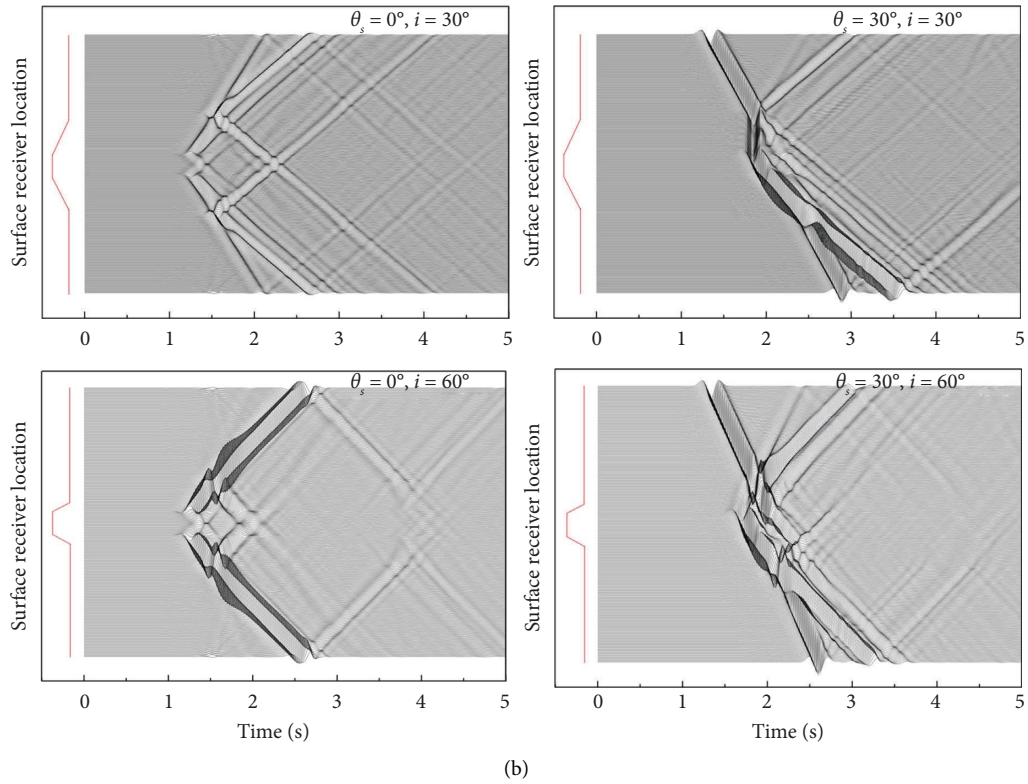


FIGURE 18: (a) Horizontal and (b) vertical acceleration seismogram synthetics for trapezoidal canyon configurations with  $i = 30^\circ$  and  $i = 60^\circ$  ( $\eta_h = 1.0$  and  $\eta_L = 1.0$ ).

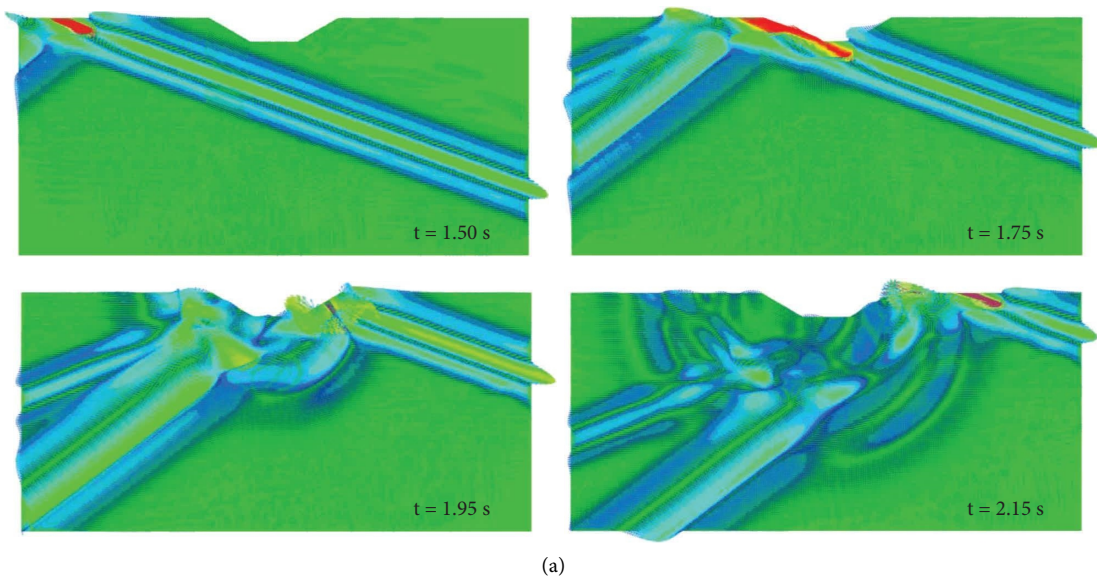


FIGURE 19: Continued.

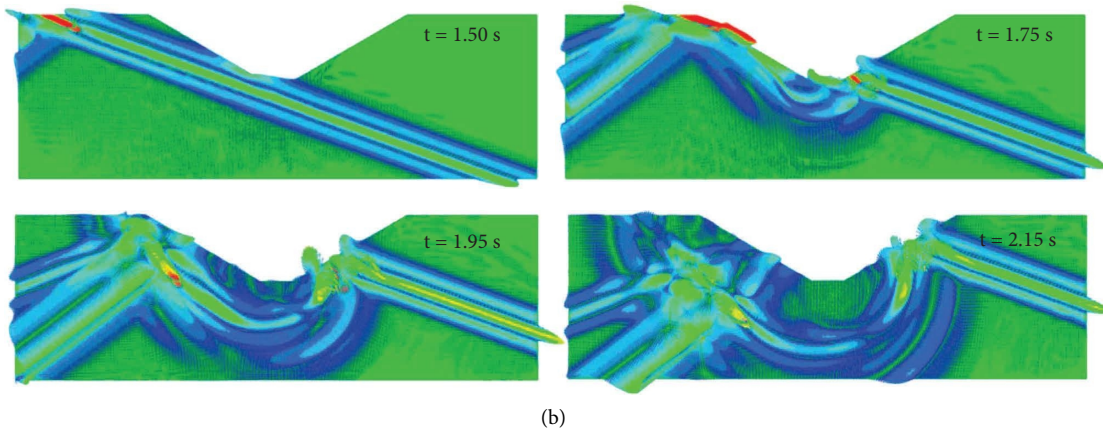


FIGURE 19: The snapshots of the acceleration wave field and the contours of absolute acceleration amplitude for canyon configurations with (a)  $\eta_h = 0.5$  and (b)  $\eta_h = 2.0$ .

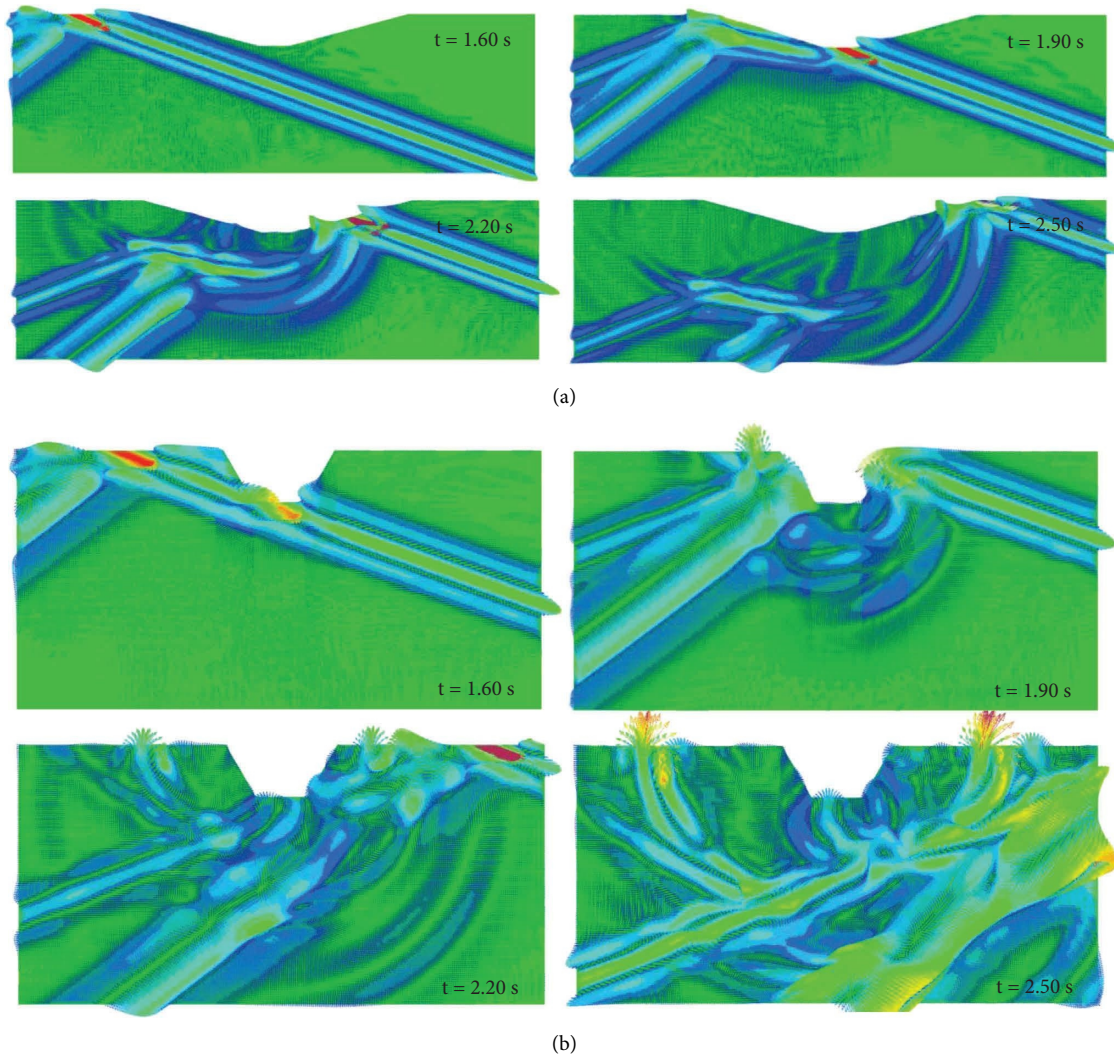


FIGURE 20: The snapshots of the acceleration wave field and the contours of absolute acceleration amplitude for canyon configurations with (a)  $i = 15^\circ$  and (b)  $i = 60^\circ$ .

inclination (Figure 20(b)), indicating that the sharper corners of the canyon can significantly distort the incident waves and reflected waves and result in stronger scattering waves. Therefore, the inclination of the canyon has a great influence on the seismic ground motions of the canyon which should be paid more attention to when performing seismic design for a canyon.

## 6. Conclusions

In this study, an input method for obliquely incident SV waves is introduced and implemented in the finite element method. The amplification factors and Fourier amplitude spectra along the trapezoidal canyon surface are then investigated. The main conclusions of this study are as follows:

- (1) The incident angle of SV waves has a significant influence on the seismic response of the trapezoidal canyon. The amplification effect may be significantly underestimated if only the vertical incidence is considered.
- (2) The horizontal amplification is greater than the vertical amplification. The horizontal and vertical amplification patterns are highly correlated with the incident angle of SV waves and the inclination of the canyon.
- (3) The effect of the inclination of the canyon on ground motion amplification is more pronounced compared to that of the canyon height and the width of the canyon bottom.
- (4) The distribution of the Fourier amplitude spectra along the canyon surface is mainly influenced by the inclination of the canyon and the incident angle of SV waves, but the dominant frequency corresponding to the acceleration at the canyon crests is not sensitive to the incident angle.

## Data Availability

The data that support the findings of this study are available from the corresponding author upon reasonable request.

## Conflicts of Interest

The authors declare that they have no conflicts of interest.

## Acknowledgments

This research was supported by the National Natural Science Foundation of China (No. 42277176).

## References

- [1] D. Assimaki, G. Gazetas, and E. Kausel, "Effects of local soil conditions on the topographic aggravation of seismic motion: parametric investigation and recorded field evidence from the 1999 Athens earthquake," *Bulletin of the Seismological Society of America*, vol. 95, no. 3, pp. 1059–1089, 2005.
- [2] D. M. Boore, "A note on the effect of simple topography on seismic SH waves," *Bulletin of the Seismological Society of America*, vol. 62, no. 1, pp. 275–284, 1972.
- [3] M. Bouchon and J. S. Barker, "Seismic response of a hill: the example of Tarzana, California," *Bulletin of the Seismological Society of America*, vol. 86, no. 1A, pp. 66–72, 1996.
- [4] J. He, S. Qi, Y. Wang, and C. Saroglou, "Seismic response of the Lengzhuguan slope caused by topographic and geological effects," *Engineering Geology*, vol. 265, Article ID 105431, 2020.
- [5] J. M. Mayoral, D. De la Rosa, and S. Tepalcapa, "Topographic effects during the september 19, 2017 Mexico City earthquake," *Soil Dynamics and Earthquake Engineering*, vol. 125, Article ID 105732, 2019.
- [6] S. A. Ashford, N. Sitar, J. Lysmer, and N. Deng, "Topographic effects on the seismic response of steep slopes," *Bulletin of the Seismological Society of America*, vol. 87, no. 3, pp. 701–709, 1997.
- [7] M. Bouchon, "Effect of topography on surface motion," *Bulletin of the Seismological Society of America*, vol. 63, no. 2, pp. 615–632, 1973.
- [8] G. D. Bouckovalas and A. G. Papadimitriou, "Numerical evaluation of slope topography effects on seismic ground motion," *Soil Dynamics and Earthquake Engineering*, vol. 25, no. 7–10, pp. 547–558, 2005.
- [9] H. Li, Y. Liu, L. Liu, B. Liu, and X. Xia, "Numerical evaluation of topographic effects on seismic response of single-faced rock slopes," *Bulletin of Engineering Geology and the Environment*, vol. 78, no. 3, pp. 1873–1891, 2017.
- [10] W. Shyu, T. Teng, and C. Chou, "Effect of geometry on in-plane responses of a symmetric canyon subjected by P waves," *Soil Dynamics and Earthquake Engineering*, vol. 113, pp. 215–229, 2018.
- [11] European Committee for Standardization, *Eurocode 8: Design of Structures for Earthquake Resistance-Part 5: Foundations, Retaining Structures and Geotechnical Aspects*, European Committee for Standardization, Brussels, Belgium, 2005.
- [12] M. D. Trifunac, "Scattering of plane SH waves by a semi-cylindrical canyon," *Earthquake Engineering and Structural Dynamics*, vol. 1, no. 3, pp. 267–281, 1972.
- [13] H. L. Wong and M. D. Trifunac, "Surface motion of a semi-elliptical alluvial valley for incident plane SH waves," *Bulletin of the Seismological Society of America*, vol. 64, no. 5, pp. 1389–1408, 1974.
- [14] V. W. Lee, "Scattering of plane SH-waves by a semi-parabolic cylindrical canyon in an elastic half-space," *Geophysical Journal International*, vol. 100, no. 1, pp. 79–86, 1990.
- [15] Y. Gao, N. Zhang, D. Li, H. Liu, Y. Cai, and Y. Wu, "Effects of topographic amplification induced by a U-shaped canyon on seismic waves," *Bulletin of the Seismological Society of America*, vol. 102, no. 4, pp. 1748–1763, 2012.
- [16] H. Kawase, "Time-domain response of a semi-circular canyon for incident SV, P, and Rayleigh waves calculated by the discrete wavenumber boundary element method," *Bulletin of the Seismological Society of America*, vol. 78, no. 4, pp. 1415–1437, 1988.
- [17] Y. Yao, T. Liu, and J. Zhang, "A new series solution method for two-dimensional elastic wave scattering along a canyon in half-space," *Soil Dynamics and Earthquake Engineering*, vol. 89, pp. 128–135, 2016.
- [18] B. Poursartip, A. Fathi, and L. F. Kallivokas, "Seismic wave amplification by topographic features: a parametric study," *Soil Dynamics and Earthquake Engineering*, vol. 92, pp. 503–527, 2017.

- [19] C. Zhao and S. Valliappan, "Seismic wave scattering effects under different canyon topographic and geological conditions," *Soil Dynamics and Earthquake Engineering*, vol. 12, no. 3, pp. 129–143, 1993.
- [20] C. Zhang, Q. Liu, and P. Deng, "Antiplane scattering of SH waves by a trapezoidal valley with a circular-arc alluvium in an elastic half space," *Journal of Earthquake and Tsunami*, vol. 09, no. 03, Article ID 1550008, 2015.
- [21] L. Yanpeng, L. Zhiyuan, H. Zhiqiang, and L. Gao, "Coupled FEM/SBFEM investigation on the characteristic analysis of seismic motions of a trapezoidal canyon in a layered half-space," *Engineering Analysis with Boundary Elements*, vol. 132, pp. 248–262, 2021.
- [22] S. A. Ashford and N. Sitar, "Analysis of topographic amplification of inclined shear waves in a steep coastal bluff," *Bulletin of the Seismological Society of America*, vol. 87, no. 3, pp. 692–700, 1997.
- [23] H. L. Wong, "Effect of surface topography on the diffraction of P, SV, and Rayleigh waves," *Bulletin of the Seismological Society of America*, vol. 72, no. 4, pp. 1167–1183, 1982.
- [24] J. Huang, X. Du, M. Zhao, and X. Zhao, "Impact of incident angles of earthquake shear (S) waves on 3-D non-linear seismic responses of long lined tunnels," *Engineering Geology*, vol. 222, pp. 168–185, 2017.
- [25] X. Du, M. Zhao, and J. Wang, "A stress artificial boundary in FEA for near-field wave problem," *Chinese Journal of Theoretical and Applied Mechanics*, vol. 38, pp. 49–56, 2006.
- [26] D. Asimaki and K. Mohammadi, "On the complexity of seismic waves trapped in irregular topographies," *Soil Dynamics and Earthquake Engineering*, vol. 114, pp. 424–437, 2018.